A High-*Q* InP Resonant Angular Velocity Sensor for a Monolithically Integrated Optical Gyroscope
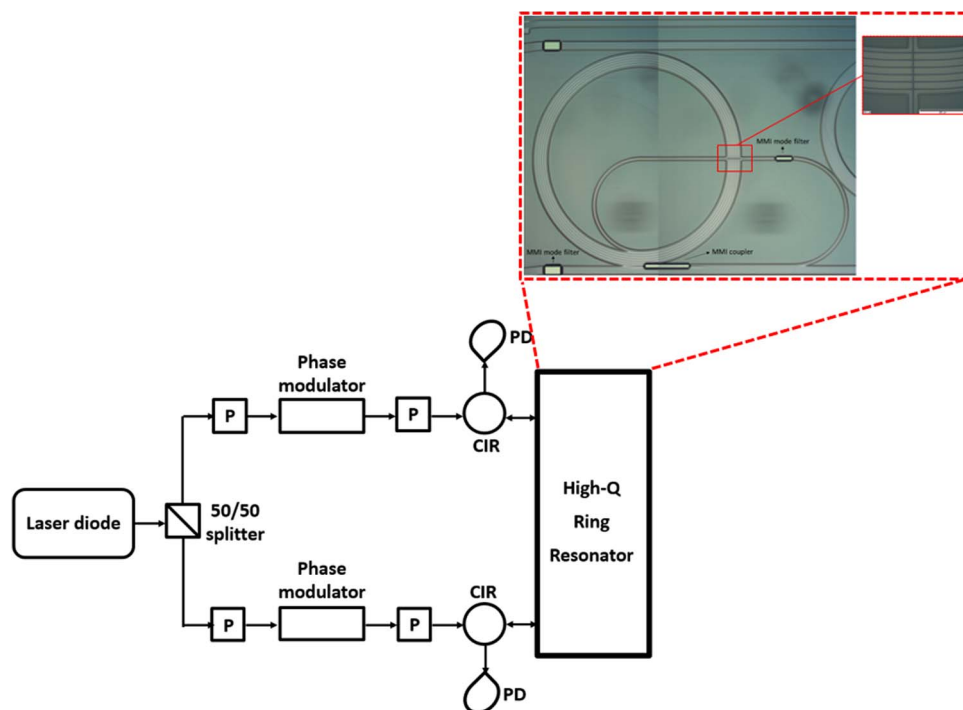
Caterina Ciminelli
Domenico D'Agostino
Giuseppe Carnicella
Francesco Dell'Olio
Donato Conteduca
Huub P. M. M. Ambrosius
Meint K. Smit
Mario N. Armenise

A High-*Q* InP Resonant Angular Velocity Sensor for a Monolithically Integrated Optical Gyroscope

Caterina Ciminelli,[2] **Domenico D'Agostino,**[1] **Giuseppe Carnicella,**[2] **Francesco Dell'Olio,**[2] **Donato Conteduca,**[2] **Huub P. M. M. Ambrosius,**[1] **Meint K. Smit,**[1] **and Mario N. Armenise**[2]

[1]Inter-University Research School on Communication Technologies Basic Research and Applications (COBRA) Research Institute, Eindhoven University of Technology, 5612 AZ Eindhoven, The Netherlands
[2]Optoelectronics Laboratory, Department of Electrical and Information Engineering, Politecnico di Bari, 70125 Bari, Italy

Abstract: The design, fabrication, and optical characterization of the sensing element of a photonic InP-based gyroscope intended for applications in the field of aerospace and defense are reported in this paper. The sensing element is a spiral resonator coupled to a straight bus waveguide through a multimode interference coupler and exhibits a *Q* factor of approximately 600000 with a footprint of approximately 10 mm^2. The design of each component of the sensor is based on some well-established numerical methods such as the Finite Element Method, the beam propagation method, and the film mode matching method. The spiral cavity was designed using the standard transfer matrix method. The selected fabrication process, which is an enhanced version of the standard COBRA process, allows the monolithic integration of the sensing element with the other active components of the gyroscope, e.g., lasers, photodiodes, and modulators. Each component of the fabricated sensing element was optically characterized using an appropriate setup, which was also used for the optical characterization of the whole sensor. Based on the results of the characterization, the gyro performance was evaluated, and a way to improve both the resolution and the bias drift, i.e., down to 10 °/h and 1 °/h, respectively, was also clearly identified. The achieved results demonstrate, for the first time, the actual feasibility of a photonic gyro-on-chip through a well-established InP-based generic integration process.

Index Terms: Integrated optics, photonic integrated circuit, generic integration process, optical resonator, gyroscope.

1. Introduction

The miniaturization of avionic components is crucial for the aerospace and defense industries, especially because it enables new on board functionalities of some complex systems that are currently a hot topic in research and development, such as unmanned air vehicles, planetary rovers, and small satellites [1], [2]. Since they are essential for the precise attitude determination of those vehicles, the demand for miniaturized gyroscopes (or gyros) with low power consumption and high reliability, also in harsh environments, is quickly growing [3], [4].

The two key figures of merit quantifying the gyros performance are the resolution, i.e., the minimum detectable angular velocity, and the drift of the bias, i.e., the sensor output when the angular velocity is zero. The most common applications in aerospace and defense demand a resolution ≤ 10 °/h and a bias drift ≤ 1 °/h.

Currently, several very reliable, high-performance gyros with resolution < 0.01 °/h and bias drift < 0.001 °/h are available on the market [5], but their size, weight, power consumption, and cost are not compliant with the requirements imposed by the above-mentioned emerging applications. Therefore, the development of miniaturized gyroscopes with resistance to radiation, vibration, mechanical shock and large thermal gradients appropriate for their military/space application is still an open technological challenge. In this context, an increasing amount of research effort is focused on the identification of new technologies that are able to face this challenge.

The use of the microelectromechanical (MEMS) technology to develop gyros for aerospace and defense has been explored in the last decade, and a three-axis vibratory gyroscope with resolution of some tens of °/h, mass of 0.75 Kg, volume < 1000 cm^3, and power consumption < 4 W is commercially available [6]. Unfortunately, this component is costly and exhibits some reliability issues, especially due to the very complex readout electronic circuit [7].

A very promising route towards miniaturized gyros is based on optical technologies. In fact, optical miniaturized gyroscopes can be realized by scaling conventional optical gyroscopes, i.e., the ring laser gyro (RLG) and the fiber optic gyro (FOG), which are currently the best performing gyro technologies (resolution from 0.01 to 10 °/h). Miniaturized optical gyros based on either semiconductor ring lasers (SRLs) or passive cavities were first proposed about four decades ago [8], [9]. They are both based on planar guided-wave cavities supporting two counter-propagating resonant modes at the same frequency when the device is at rest, while suffering from a splitting induced by the Sagnac effect [10] under rotation.

In the SRL-based gyros [11]–[13], the resonant waves are generated within the cavity which also acts as a sensing element. They have a small footprint (< 1 cm^2), low power consumption and can be easily integrated on a single chip, but their performance is limited by backscattering and mode competition within the active cavity and a significant dithering is required to ensure a flawless sensor operation.

Optical angular velocity sensors based on passive ring resonators are less compact and have a more complex configuration with respect to the SRL gyros. However, they show the fundamental advantage of being immune to the above-mentioned non-linear effects.

In this class of resonant optical gyros (ROGs), passive ring resonators are used as the sensing element. Two counter-propagating resonant modes at the same resonance frequency are excited in the ring by a narrow line width external laser. Under rotation, a difference Δf in frequency between the resonant modes, which is proportional to the angular rate Ω, is generated due to the Sagnac effect. The difference in frequency is measured through a closed-loop readout optoelectronic system, based on phase or frequency modulation spectroscopy [14]–[19].

The shot-noise limited resolution $\delta\Omega$ of the ROGs strongly depends on the resonator quality factor Q and on the ratio between the resonator perimeter P and the area A enclosed by the light path within the optical cavity. It can be expressed as

$$\delta\Omega = \frac{P \cdot c}{A \cdot Q} \sqrt{\frac{Bhf_s}{8\eta_{pd}P_{pd}}} \tag{1}$$

where c is the speed of light in vacuum, f_s is the sensor operating frequency, B is the sensor bandwidth, h is Planck's constant, P_{pd} is the average optical power at the photodiodes input, and η_{pd} is the quantum efficiency of the photodiodes.

From (1), it can be easily derived that the resolution can be improved by maximizing the product $A \cdot Q/P$ and/or increasing P_{pd}. The quality factor mainly depends on the propagation loss within the optical cavity, whereas the ratio A/P is enhanced by increasing the resonator size. The parameter A/P quantifies the gyro sensitivity to rotation. P_{pd} depends on both the laser

power and the total loss suffered by the optical beams along their path from the laser to the photodetectors. Therefore, the resonators used as sensing elements of the ROGs must be large-area cavities (footprint of the order of 1–10 cm^2) with high Q values ($Q \geq 10^6$) realized by using either optical fibers [20] or low-loss integrated optical technologies [21], [22]. A resolution ≤ 10 °/h, which is required by most of the applications in the field of aerospace and defense, can be achieved by resonant micro optical gyros (RMOGs).

Resonant fiber-optic gyroscopes (RFOGs) have been demonstrated to have a resolution less than a few tens of °/h [23]–[28], but their miniaturization is prevented by the bending loss in the fiber resonators. In fact, for this reason, the size of the RFOG sensing element is typically > 40 cm^2.

A resolution of the order of some hundreds of °/h with a reduced footprint has been reported [29] for RMOGs, even if further improvements are needed to achieve a resolution ≤ 10 °/h.

Two technological approaches are being explored to implement RMOGs, i.e., the hybrid integration of several optoelectronic components in different substrate materials and the monolithic integration of all components on a single chip [30].

In this paper, we explore the former approach by reporting on the design, fabrication and testing of a high-Q InP spiral resonator, with a length of 60 mm and a footprint of about 3.0 mm $\times$ 4.2 mm, to be used as sensing element of a fully integrated InP gyroscope with a target resolution ≤ 10 °/h.

2. Monolithic Integration of Optical Gyroscopes

Monolithic integration will allow all optoelectronic components of the gyroscope to be integrated on a single chip, greatly decreasing the device size and increasing its immunity to external disturbances, such as vibration or thermal stress.

Generic InP-based platforms enable the fabrication of qualified photonic integrated circuits by co-integrating *active* building blocks, such as lasers, photodiodes, and phase modulators, together with *passive* waveguides and waveguide components.

Numerous complex InP-based photonic integrated circuits have been successfully demonstrated [31] but, the fabrication of high-Q InP integrated cavities is challenging due to the typical waveguide propagation loss > 1 dB/cm.

Although waveguide loss is one of the most important performance parameters of photonic integration platforms, the monolithic integration of active and passive sections typically increases optical losses to a level that is not suitable for high-resolution gyros.

The main foundries offering a generic integration process are the U.K.-based company Oclaro, the Fraunhofer Heinrich Hertz Institut in Berlin, Germany, and the COBRA Institute in Eindhoven, the Netherlands whose process is now commercialized by the spinoff company SMART Photonics.

All the above-mentioned foundries make use of a multi-step technological process, including epitaxial growth of the multi-layer structure, waveguide etching, passivation/planarization, and metallization.

The processes at COBRA and Oclaro are quite similar and are both based on the use of an n-doped InP substrate, enabling the easy integration of optical amplifiers and laser diodes. The Oclaro process does not allow low-loss (< 1 dB/cm) waveguides and devices. To improve the radio frequency performance of some devices and to enable the electrical isolation of individual devices, the process of Fraunhofer uses a semi-insulating (Fe-doped) substrate. Therefore, up to now, it does not support the integration of optical amplifiers or laser sources.

By considering the process using the Fe-doped substrate, an InP ring resonator was designed and fabricated with a radius of 1.3 cm and a total length of 8.16 cm, evanescently coupled to a straight bus waveguide [32], [33]. A quality factor equal to 0.97×10^6 was experimentally demonstrated. The value of the ring radius was chosen in order to allow the cavity to be placed in 1/4 of the 3-inch InP wafer with the aim of assuring an appropriate uniformity of the technological process. Particular care was devoted to the choice of the waveguide structure, selecting an

InGaAsP/InP rib waveguide with width equal to 2 μm and etch depth equal to 0.3 μm, as a trade-off between the scattering loss reduction and the bending loss minimization [33]. The measured propagation loss of the fundamental quasi-TE mode supported by the single-mode guiding structure, was 0.45 dB/cm. For the gyro based on this InP resonator, a target resolution of 10 °/h was numerically evaluated by assuming an optical power at the detector P_{pd} equal to 14 mW [33]. Due to the use of the semi-insulating substrate, the process using the semi-insulating substrate allows easy manufacturing of low loss passive devices, but their monolithic integration with active devices, such as laser diodes, is challenging.

The process reported in [34] involves three epitaxial steps. In the first growth step, the active region including the lower part of the p-doped cladding is grown. Subsequently, the active regions are masked and the exposed areas are selectively etched away. In the second step, a selective re-growth is applied to obtain transparent waveguide sections. In the transparent section, the cladding layer is un-doped to avoid absorption losses. In a third step, the whole structure is covered with a p-doped cladding layer increasing the optical loss in the passives.

A variation of this process has recently been introduced [35], [36] and is based on the local diffusion of Zinc (Zn-) to define p-doped regions only in the active regions. This has resulted in a reduction in the loss of shallowly-etched waveguides (medium index contrast) from 2 dB/cm to 0.4 dB/cm. For a spiral ring resonator with a length of 73 mm using the low loss waveguide, a record quality factor of 1.2×10^6 with an extinction ratio of about 10 dB has been measured in TE polarization [35], [36]. This value has increased the state-of-the-art [33] by about 20% and was an important step towards generic PICs for demanding sensing applications, such as optical gyroscopes.

After the improvement in terms of propagation loss, as reported in [35], [36], the COBRA process appears the most appropriate for the monolithic integration of lasers, modulators, and photodiodes with low loss passive devices, such as a ring resonator. For this reason, we selected it for fabricating a spiral resonator proposed as the sensing element of an InP fully integrated photonic gyroscope, as described in the following section. The achievements reported in this paper demonstrate that a photonic gyro-on-chip for aerospace and defense applications is feasible through the COBRA process, which has recently been enhanced by the local Zn-diffusion [35], [36].

3. Design of the Optical Components of the Angular Velocity Sensor

The design details of the optical components of the sensing element are described in this section. The sensing element is a ring resonator coupled to a straight bus waveguide through a multi-mode interference (MMI) coupler. The waveguide configuration for the planar cavity fabrication has been properly selected and numerically investigated. Since the guiding structure is not single-mode, a mode filter has been included in the resonant path to suppress higher order modes. The sensor operating wavelength is 1.55 μm ($f_s = 193$ THz).

3.1. Waveguide

A shallowly etched waveguide according to the COBRA process is depicted in Fig. 1 and has been selected for the resonator fabrication. A record propagation loss of 0.3 dB/cm has been reported for this structure [36].

The model proposed by Fiedler $et\ al.$ [37] was used to evaluate the refractive index of each material, and that by Walukiewicz $et\ al.$ [38] for the absorption loss. Fig. 1 also reports both real and imaginary parts of the materials refractive index, for the specific doping concentrations.

The waveguide modes were computed by using a full-vector complex mode solver based on the Finite Element Method (FEM) and the results were also confirmed by the Beam Propagation Method (BPM). The waveguide supports both fundamental TE (TE_0, $n_{effTE_0} = 3.275 + i7.643 \times 10^{-7}$) and TM modes ($TM_0$, $n_{effTM_0} = 3.269 + i8.421 \times 10^{-7}$) and two higher order modes (TE_1 and TM_1, $n_{effTE_1} = 3.246 + i9.158 \times 10^{-7}$, and $n_{effTM_1} = 3.240 + i9.744 \times 10^{-7}$, respectively), as shown in Fig. 2.
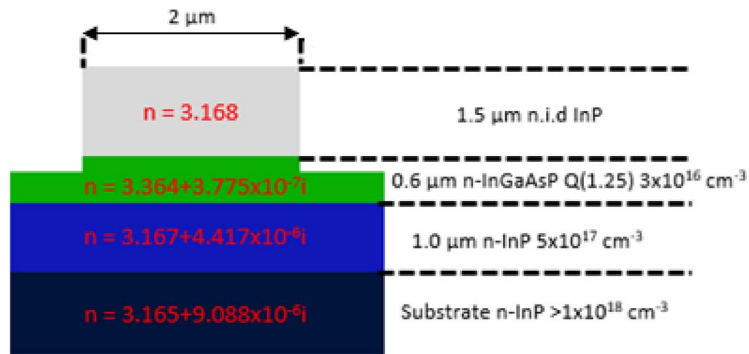
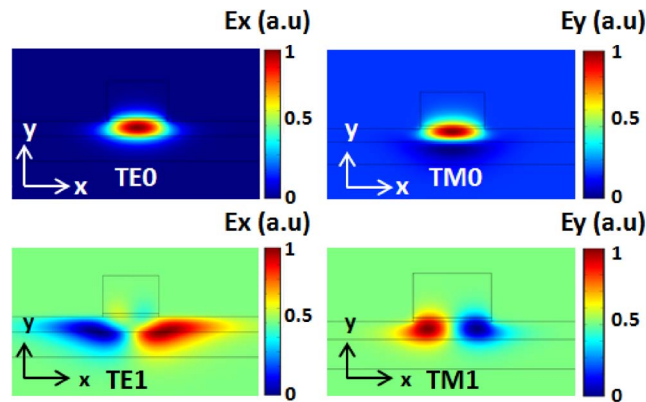Fig. 1. Configuration and optical properties of the shallow waveguide in InP/InGaAsP.

Fig. 2. Modal analysis of the shallow waveguide.

The imaginary part k of the effective index was used to evaluate the optical loss in the waveguide, by using the following equation:

$$\alpha = \frac{4\pi k}{\lambda}. \tag{2}$$

For the fundamental TE_0 mode the optical losses were calculated to be equal to 0.27 dB/cm at 1.55 μm, without considering the scattering loss. The TM_0 absorption loss is 0.30 dB/cm at 1.55 μm, a bit higher than that of TE_0. The absorption loss of the fundamental TE_0 mode increases from 0.26 dB/cm to 0.29 dB/cm as the wavelength increases from to 1.45 μm to 1.65 μm.

The radiation loss due to the waveguide bending was evaluated using the film mode matching method. The asymmetry in the field distribution can be reduced by the choice of larger bending radii.

Fig. 3(a) shows the excess loss only due to bending as a function of the bending radius for the fundamental TE mode. As expected, the excess loss decreases as the radius increases. The modal distribution of the fundamental TE for a bending radius of 400 μm is shown in Fig. 3(b). The excess loss for this bending radius is 0.003 dB/cm, which can be neglected as it is two orders of magnitude below the free carrier absorption. With a bending radius of 1200 μm the TE_0 mode has a symmetric distribution [see Fig. 3(c)] comparable to the straight configuration. For a bending radius of 400 μm, the TE_1 mode has an excess loss due of approximately 100 dB/cm. The TE_1 excess loss decreases as the bending radius increases. It is 0.004 dB/cm for a radius of 1200 μm.
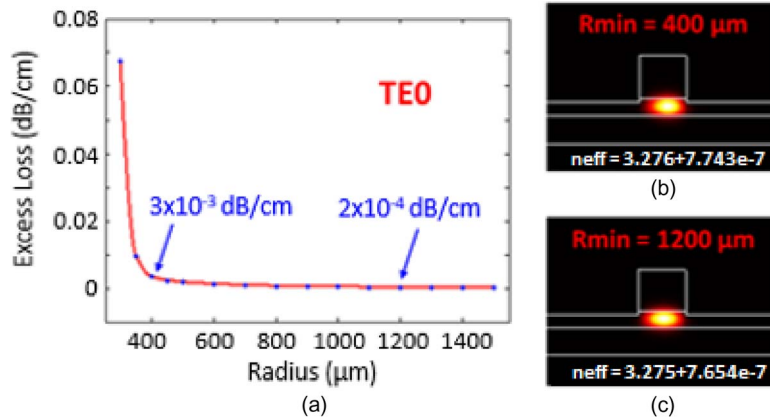
Fig. 3. Excess loss vs. radius for TE_0 mode (a). Modal distribution related to TE_0 in the shallow waveguide with a bending radius of 400 μm (b) and 1200 μm (c).
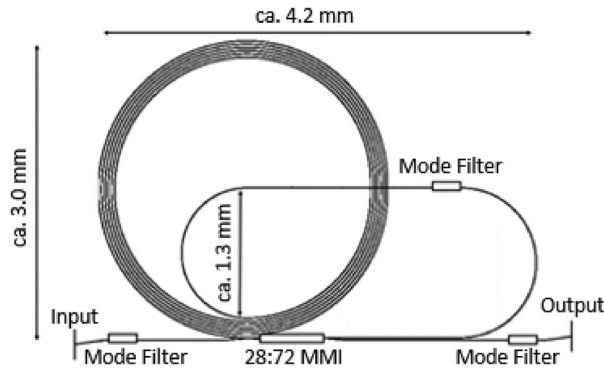

Fig. 4. Designed spiral resonator.

3.2. Resonator Configuration and Design Criteria

The theoretical spectral response of the planar cavity, which is a ring resonator with a spiral configuration (see Fig. 4), has been derived by using the transfer matrix method. The spiral configuration selection is discussed at the end of this sub-section. As already mentioned, a mode filter is included in the resonant path. Two additional mode filters are located at the two ends of the straight bus waveguide.

The performance parameters we considered for the design of the resonator to be used as the sensing element of the RMOG with a target sensitivity $\leq$ 10 °/h were the quality factor Q and the extinction ratio ρ. They can be expressed, respectively, as

$$Q = \frac{\pi n_g L \sqrt{ra}}{\lambda_{\text{res}}(1 - ra)} \tag{3}$$

$$\rho = \frac{(r + a)^2(1 - ra)^2}{(1 + ra)^2(r - a)^2} \tag{4}$$

where n_g is the group index of the material, L is the resonator length, λ_{res} is the resonance wavelength, and r is the coupling coefficient, i.e., the fraction of the input field amplitude remaining in the bus waveguide. The parameter a takes into account the propagation loss and is expressed as $a = e^{-\alpha L}$, where α includes all loss contributions within the ring, i.e., propagation loss of the waveguide, insertion loss of the coupler, and radiation loss due to the bends.
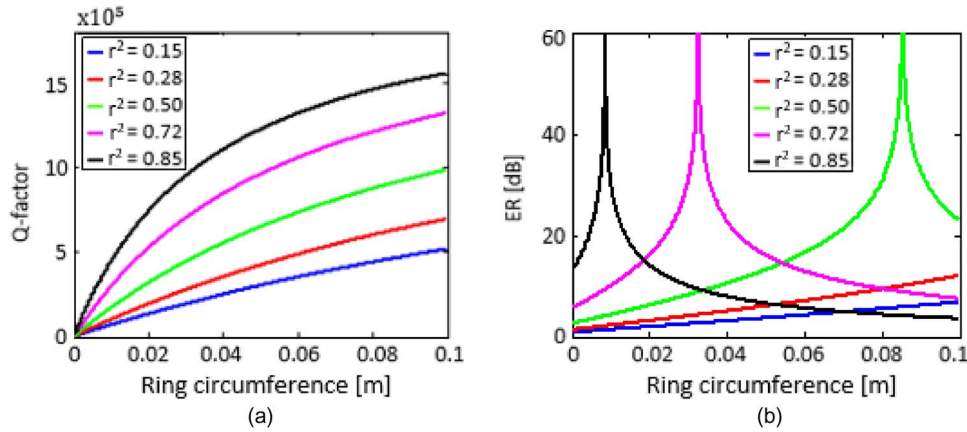
Fig. 5. Quality factor (a) and extinction ratio (b) as functions of ring length for different coupling ratios.

To enhance the device quality factor, the selected cavity configuration includes just one bus waveguide instead of two. A quality factor of 10^6 and an extinction ratio of 7 dB are the ring target performance.

The quality factor is proportional to the length L of the ring resonator [see (3)]. The coupling coefficient, r, and the parameter a also have to be maximized to achieve high values of Q.

We simulated the dependence of both quality factor and extinction ratio on different coupling ratios to match our design target. The Q-factor and extinction ratio trends as functions of the ring length are shown in Fig. 5(a). A propagation loss coefficient of 0.3 dB/cm, a coupler loss equal to 0.5 dB, and five different coupling ratios were assumed.

In order to obtain a Q-factor close to one million, a coupling ratio r^2 of 0.72 and 0.85 have to be considered for a ring length longer than 54 mm and 33 mm, respectively. To achieve this performance, a spiral configuration is proposed, with the aim of reducing the resonator footprint and ensuring a good uniformity of the fabrication process. Numerical simulations allowed us to conclude that for a coupling ratio equal to 0.85, ρ is very sensitive to the propagation loss increase. Therefore, we chose $r^2 = 0.72$, which allows for a higher ρ even if the Q-factor is slightly lower. The Q-factor exceeds one million for a propagation loss of 0.3 dB/cm and a ring length longer than 50 mm.

3.3. Coupler and Mode Filter

An MMI coupler was preferred to the directional coupler due to relaxed fabrication tolerances and low insertion loss [39].

The basic element of an MMI coupler is a wide multi-mode waveguide, where a set of modes propagate and interfere constructively with the imaging length, to form a self or split image at the output. According to the theory [40] for a 2 × 2 coupler, a device length equal to $L_{2\times2} = 9L_\pi/5$ was chosen to produce an asymmetric splitting ratio of 28:72. L_π is the beat length of the two lowest order modes defined as $L_\pi = (\pi/\Delta\beta) \sim 4n_{\text{reff}}w^2/3\lambda$, where $\Delta\beta$ is the difference between the propagation constants of the two lowest order modes, W and n_{reff} are the width and the effective refractive index of the multimode ridge. The behavior of the MMI coupler was evaluated by 2-D BPM simulations in [36]. Here some results achieved by 3-D BPM are reported. The MMI coupler configuration is depicted in Fig. 6, where the cross-section of the waveguides forming the input guiding structures and the MMI section are shown.

The values of the splitting ratio of the MMI coupler by 3-D BPM simulations, shown in Fig. 7, confirmed the results previously obtained from the theoretical model.

A tapering section with an angle $\theta = 54°$ (see Fig. 8) was included at both input and output section of the MMI device to reduce back reflections.
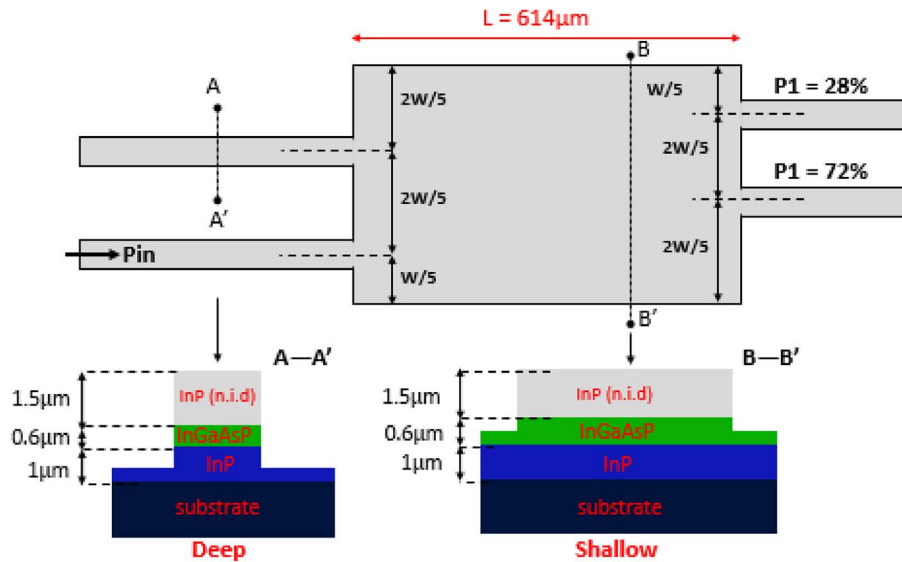
Fig. 6. Configuration of the 3-D MMI coupler with a deep waveguide in InP/InGaAsP, without tapered sections.
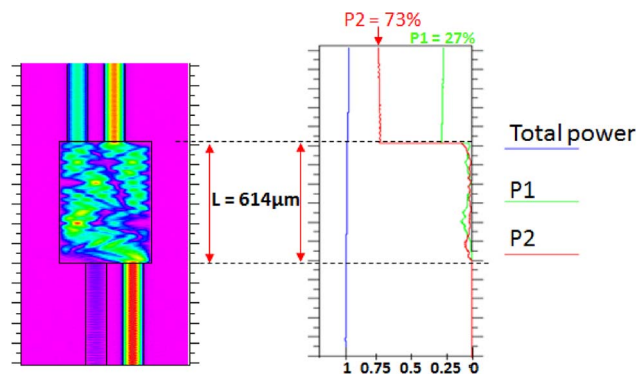

Fig. 7. Three-dimensional BPM simulations of the MMI coupler without the input taper (left) and its power splitting ratio (right).

The insertion loss in the MMI with the tapering sections at both input and output sections of the device was calculated to be equal to 0.1 dB.

From the e.m. analysis (see Section 3.1.), we concluded that the waveguides support both the zero- and first-order guided modes. A 1×1 MMI coupler has been used as a mode filter to suppress the first order mode, so avoiding modal interferences. The fundamental mode should pass unaltered through the filter while the higher order mode should be suppressed by it. The device length is defined by $L_{1x1} = 3L_\pi/4$. For the TE mode, 2-D BPM simulations were performed to find the optimal 1×1 MMI coupler length for multimode waveguide widths ranging from 5.0 to 10.0 μm, at 1550 nm. The 1×1 MMI coupler insertion loss was evaluated as a function of the wavelength. Larger waveguides are more sensitive to wavelength changes. At 1550 nm, the MMI insertion loss is negligible.

Fig. 9 shows the transmission of the 1×1 MMI coupler on the first-order mode TE_1 as a function of the wavelength, at six values of the waveguide width. The attenuation increases for wider waveguides. The 10 μm-wide and 211 μm-long 1×1MMI coupler gives approximately 15 dB of attenuation for the first-order mode from 1500 to 1600 nm.
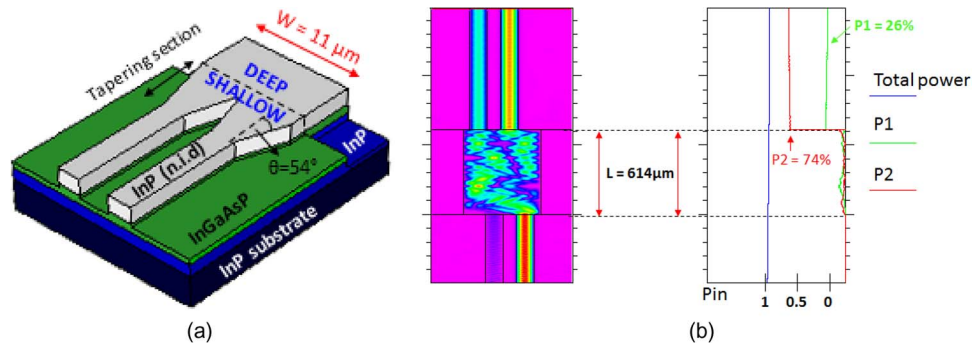
Fig. 8. (a) Input of the MMI coupler with a tapering section. (b) 3-D BPM simulations of the MMI coupler behavior with the input taper (left) and splitting ratio (right).
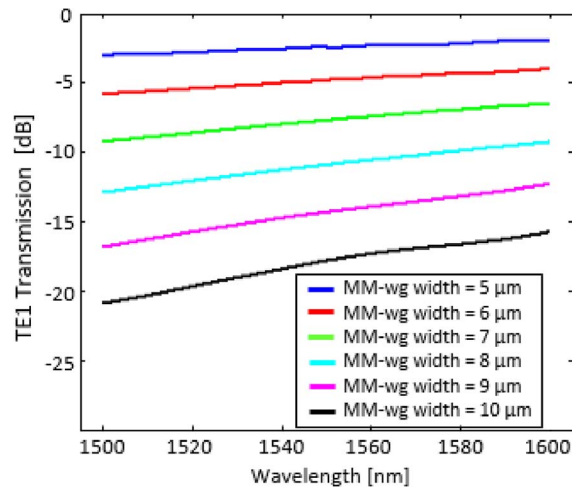

Fig. 9. TE$_1$ mode transmission as a function of the wavelength for several waveguide widths.

A further improvement in the 1×1 MMI coupler performance can be obtained by angled side-walls at the input and output of the MMI structure. 2-D BPM simulations were performed for the 10 μm-wide 1×1 MMI coupler, for several values of ϑ, showing that the suppression of the first-order mode increases as ϑ decreases from 90° down to 35°. A value of $\theta = 45°$ was so fixed for the device fabrication. A theoretical insertion loss of 0.1 dB was predicted for the filter.

3.4. Spiral Resonator

A spiral configuration was chosen for realizing the resonator structure. The spiral configuration ensures a quality factor around one million, reducing at the same time the device footprint.

We designed a six coil spiral that allows for a 60 mm long resonator with a footprint of approximately 3.0 mm $\times$ 4.2 mm, potentially suitable for an RMOG with a target resolution $\leq$ 10 °/h. The distance between two spiral coils is of approximately 25 μm to avoid any coupling between them. Angled waveguides at the input and output of the ring were used to reduce optical reflections.

As discussed above, a first-order mode filter consisting of 1×1 MMI couplers was placed inside the ring. The mode filter gives a further contribution to the roundtrip loss, which adds to the propagation loss of the waveguide, the radiation loss due to bends, the reflections caused at waveguide junctions, and the MMI insertion loss. The radiation loss can be considered negligible due to the choice of a minimum radius close to 500 μm. The waveguide junctions were
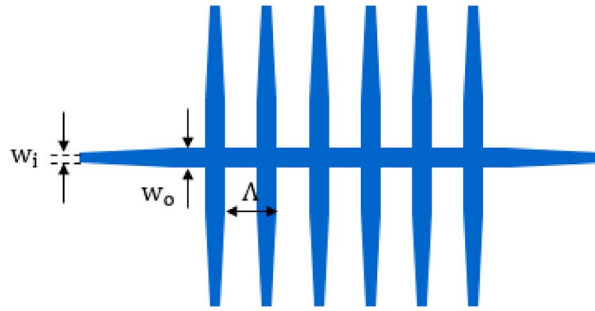
Fig. 10. Crossing geometry in the ring resonator.

optimized by the introduction of a lateral offset and their cumulative loss is roughly 0.1 dB. MMI couplers were designed to minimize the insertion loss. In order to reduce reflections, angled waveguides at the input and output of the resonator were also considered.

The spiral configuration includes closely spaced crossing waveguides (see Fig. 10). The design of the crossings is based on the excitation of a low-loss Bloch wave in the periodic structure [41].

The low loss Bloch mode is generated by the superposition of the zero- and second-order mode [41] with a precise ratio between their amplitudes. The design approach allows us to achieve the minimum optical field value at the crossing point. To design a low loss crossings array, the waveguide width, the taper width and length and the crossings periodicity have to be optimized. The waveguide and the taper were designed to excite the second-order mode.

The crossing periodicity Λ is determined by matching the difference in propagation constants of the zero- and second-order mode (β_0 and β_2, respectively), according to the following equation [41]:

$$\Lambda = \frac{2\pi}{\beta_0 - \beta_2} = \frac{\lambda}{n\text{eff}_0 - n\text{eff}_2}. \tag{5}$$

The minimum waveguide width w_0 to excite the second-order mode was calculated to be equal to 3.1 μm. At the same time, we have to avoid the excitation of the third-order mode, which needs a width w_0 less than 4.6 μm. The effective refractive indexes of the zero- and the second-order modes ($n\text{eff}_0$ and $n\text{eff}_2$, respectively) used to calculate the crossings spacing Λ accordingly to (5) at 1550 nm were evaluated, showing an increase of the crossings spacing as w_0 increases.

The design of the tapers, in which the waveguide width passes from w_i to w_0, was aimed at the excitation of the second-order mode, minimizing the insertion loss. We carried out 2-D BPM simulations to evaluate the taper insertion loss as a function of the taper length for several output widths. The taper has very low loss for lengths greater than 40 μm, as shown in Fig. 11(a). We also estimated the second-order mode transmission at the taper output. Simulated trends are shown in Fig. 11(b). For each output waveguide width w_0, we obtained the optimal taper length and the corresponding second-order mode transmission.

The best performance is expected for $w_0 = 3.5$ μm and a crossings spacing $\Lambda = 32$ μm. The selected length for the two tapers is 40 μm. At 1550 nm, an insertion loss of 0.13 dB was evaluated for the TE polarization in the six crossing structure.

3.5. Other Components Necessary to Achieve a Fully Integrated System

The configuration of the InP photonic section of the gyroscope under study is shown in Fig. 12.

The key component is the high-Q resonator, which is the element sensitive to rotation and the Q-factor and size of which determine the sensor resolution. The phase modulators have an important role in the sensor readout circuit, which is based on the phase modulation spectroscopy,
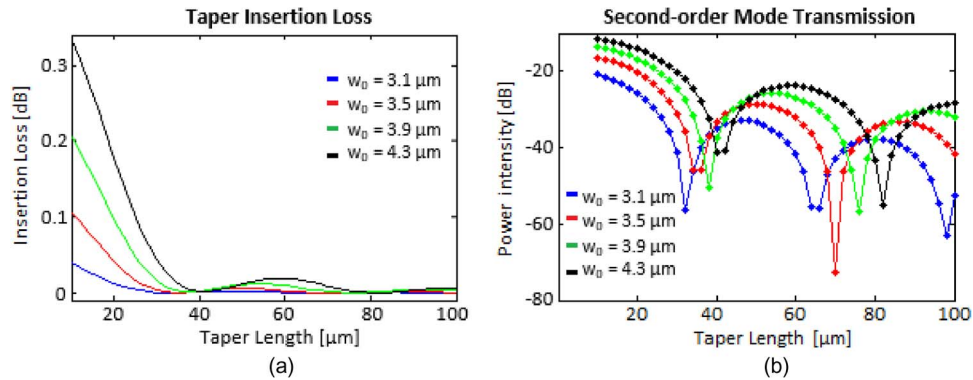
Fig. 11. (a) Taper insertion loss and (b) power intensity of the second-order mode as function of the taper length for several output widths.
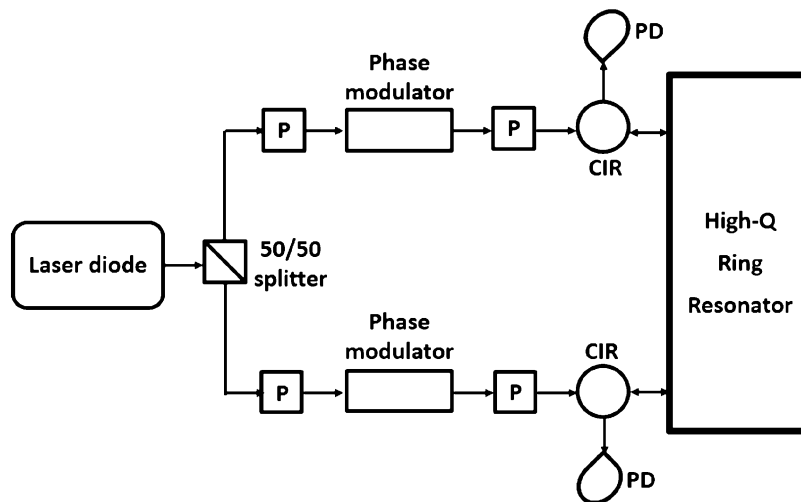

Fig. 12. Configuration of the InP photonic gyroscope. P: polarizer. CIR: circulator. PD: photodiode.

and the features of their driving signals must be properly optimized to suppress the gyro noise sources [42].

Some of the other components, i.e., the laser diode, photodiode, electro-refractive phase modulator, and 50/50 splitter, have been available on the COBRA platform for several years and are well optimized [31]. The coupled-cavity laser diode [43], [44] fabricated by the COBRA platform, having a linewidth of about 1 MHz, is the most appropriate for the specific application. The phase modulator consists of a reversely biased p-i-n junction in which the phase modulation is mainly due to the carrier depletion in the waveguide layer. The bandwidth of the modulator is 10 GHz, its half-wave voltage is 7 V, and its length is 2 mm. The photodiode has the same bandwidth of the modulator, a dark current < 20 nA, and a length < 1 mm. The 50/50 splitter is based on a properly optimized MMI.

Some building blocks for polarization handling, such as polarization converters and splitters, have been already demonstrated at COBRA [45] and will be integrated in the COBRA platform very soon. By using those building blocks, the polarizer can be easily integrated into the gyroscope.

The circulator is not currently available on the COBRA platform, but a simple three-port circulator based on two ring resonators and a Y-branch has been recently demonstrated in silicon
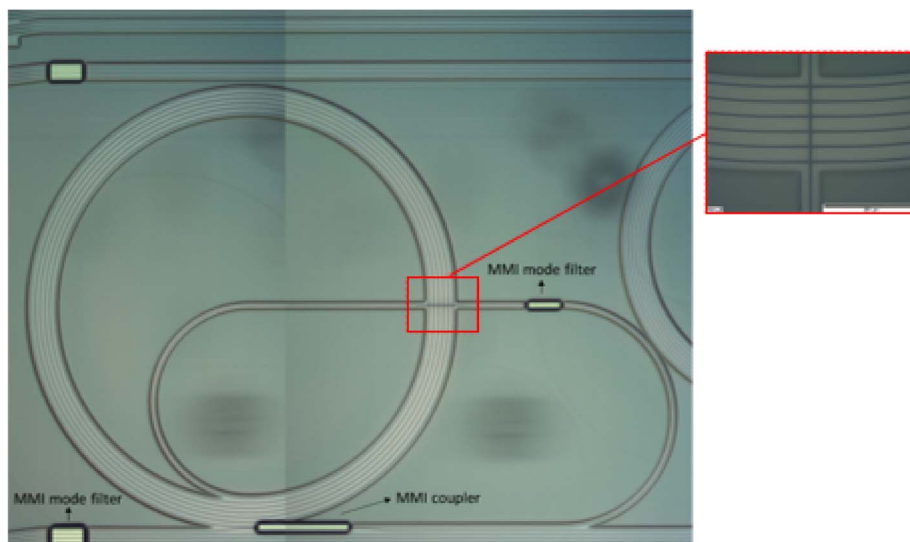
Fig. 13. Fabricated ring resonator. (Inset) Waveguide crossing.

technology [46] and could be easily implemented in InP technology from the basic building blocks already available on the COBRA platform, which would lead to the manufacturing of the first monolithically integrated InP optical gyros. The lack of the circulator in the selected technological platform could be a critical aspect in the demonstration of the gyro-on-chip.

4. Optical Characterization

As already mentioned, the gyro sensing element has been fabricated using the COBRA standard process, as modified by including a local Zn-diffusion step [36]. One of the fabricated devices is shown in Fig. 13, together with the detail of the waveguide crossing.

Before the characterization of the gyro sensing element, some test-structures were characterized to evaluate the performance of the sub-components.

The waveguide loss was measured by the Fabry-Perot method [47] with a tunable laser, where the lasing wavelength was changed from 1540 nm to 1550 nm with a step size of 0.1 pm. Propagation losses equal to 0.3 dB/cm $\pm$ 0.1 dB/cm and to 0.4 dB/cm $\pm$ 0.1 dB/cm, were found for TE and TM polarization, respectively, [36].

The Fabry-Perot method was also used to test the 2 $\times$ 2 MMI coupler. The insertion loss was estimated to be 0.1 $\pm$ 0.1 dB at 1510 nm and 0.2 dB at 1545 nm for the TE and TM polarization, respectively. Those values match the numerically predicted ones. The coupling coefficients were also extracted from the measurements [36], showing that $r^2 = 0.72 \pm 0.02$ is achieved at the point of minimum insertion loss for both TE and TM polarizations.

The 1 $\times$ 1 MMI coupler characterization was also based on the Fabry-Perot method. We derived the device insertion loss by using concatenated mode filters. The insertion loss trend for TE polarization in Fig. 14(a) shows a good agreement between measured and simulated values. The minimum insertion loss is shifted towards 1500 nm, which is due to a variation in the definition of the MMI width of 250 nm. The insertion loss trend for TM polarization, shown in Fig. 14(b), is shifted up with respect to the simulations and has a 60 nm-wide bandwidth where the insertion loss value is less than 0.4 dB.

Six-crossing test structures with 1, 5, and 10 concatenated crossings were characterized. Fig. 15 shows the measured insertion loss, which is increasing as a function of the wavelength. At 1510 nm, the insertion loss is about 0.4 dB for the TE polarization. This experimental value exceeds the numerical result of approximately 0.3 dB.
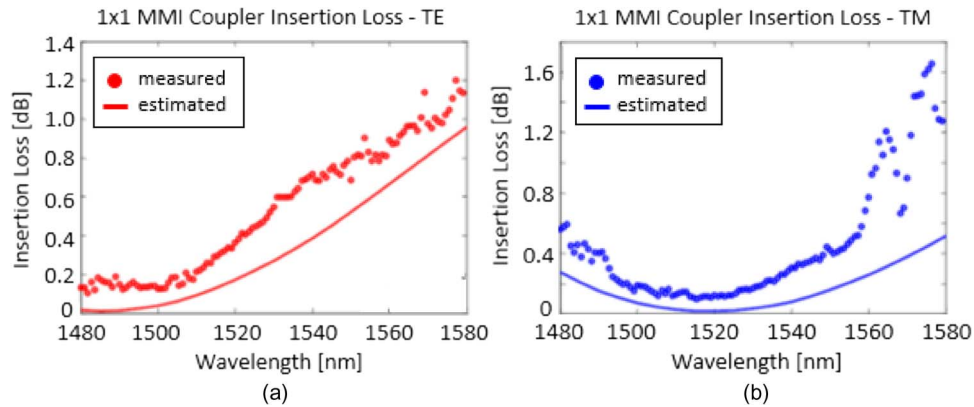
Fig. 14. Comparison between measured and estimated insertion loss as a function of the wavelength for (a) TE and (b) TM polarization.
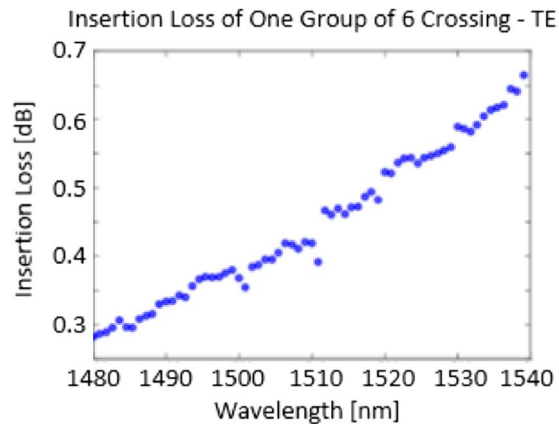

Fig. 15. Insertion loss of one group of six crossings for TE polarization.

Based on the experimental results of the characterization of each sensor component, we can conclude that the total roundtrip loss is about 2.6 ± 0.6 dB, from which 1.8 ± 0.6 dB is due to absorption and scattering loss in the waveguide, 0.4 dB to the coupler and the mode filter, and 0.4 dB to the six crossings.

The experimental results achieved for all components of the resonator suggest that the resonators based on these components should perform close to ideal around 1510 nm for TE and 1540 nm for TM polarization, respectively.

The spiral resonator was characterized by using the setup depicted in Fig. 16. A tunable laser was coupled via a collimating lens to free space. After passing through a polarizer, the collimated beam was coupled into the device by a microscope objective. A polarization controller was used to maximize the transmission through the polarizer set to TE or TM. To evaluate the spectral response, the sensing element was excited by the laser source whose emission frequency was continuously tuned at a speed of 500 pm/s. The oscilloscope allows the transmitted optical power at output to be recorded in real time, while the laser is swept, with a sampling frequency of 100 kHz. Considering the laser sweep speed and the oscilloscope sampling frequency, the wavelength resolution is 5 fm.

The lasing wavelength was set at 1510 nm for TE and 1540 nm for TM.

Each experimental transmission peak in a free spectral range was separated and fit to the theoretical ring transmission to obtain the extinction ratio and the Q-factor. The propagation loss was assumed to be equal to 0.3 dB/cm in the fitting algorithm. The normalized spectral response
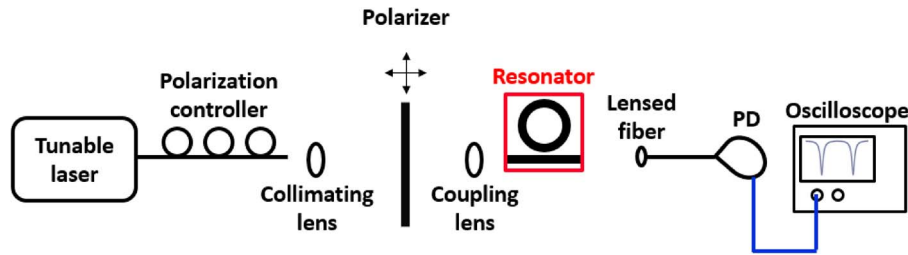
Fig. 16. Experimental setup for characterizing the fabricated spiral resonator.
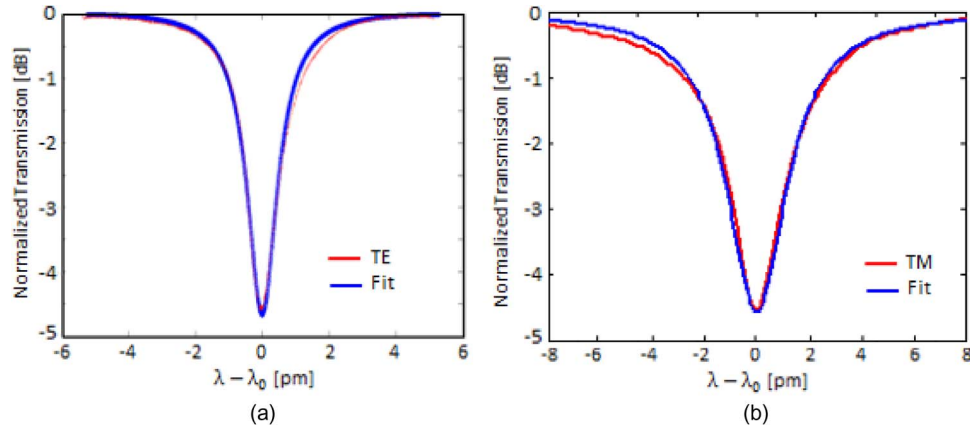

Fig. 17. Ring resonator spectrum for the TE (a) and the TM (b) polarization. Lineplots represent the fit to the theoretical equations.

of the cavity with a length $L = 60$ mm and a coupling ratio $r^2 = 0.72$ is shown in Fig. 17 for the TE and the TM polarization.

The total spiral loss is 3.2 dB for TE polarization and 3.0 dB for TM polarization. These values agree with the prediction based on the experimental characterization of the sensor basic components and are higher than the simulated ones, probably due to scattering and further reflection contributions due to the crossings. The extinction ratio values are 4.8 dB for TE polarization and 4.5 dB for TM, with a Q-factor of 5.90×10^5 and 4.95×10^5, respectively. The resonator finesse is 3.9 for the TE polarization and 3.5 for the TM one.

The crossings surely introduce an additional loss contribution to the spiral. A lower quality factor has been achieved, if compared with the longer resonator in [36] due to higher path losses and the shorter length. In addition, the cavity in [36], due to its configuration without crossing, has a low sensitivity to rotation because only the outer waveguide contribute to the Sagnac effect, while the contribution of the inner waveguides cancels it out.

5. Gyro Performance Discussion

Data provided by the experimental characterization of the fabricated sensing element allows the estimation of the two key performance parameters of our sensor prototype, i.e., the sensor resolution (or minimum detectable angular velocity) and the bias drift.

By considering (1) and by assuming $B = 1$ Hz, $P_{pd} = 20$ mW, and $\eta_{pd} = 0.9$, we have plotted, in terms of level curves, the gyro resolution depending on Q and the A/P ratio (see Fig. 18).

The curves show that the resolution improves as Q and/or the A/P ratio increases. The red level curve specifies the values of Q and A/P allowing achievement of the target resolution (10 °/h). A Q-factor > 850 000 and a ratio A/P > 3.2 mm are required to achieve the resolution value of 10 °/h.
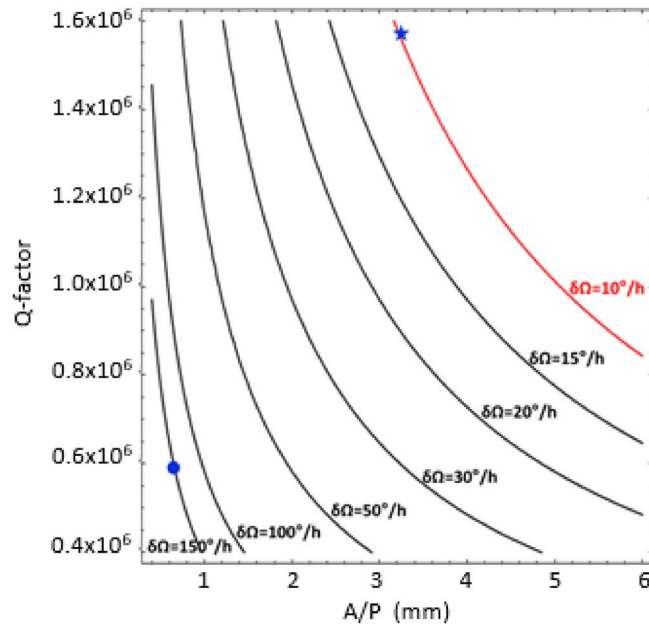
Fig. 18. Gyro resolution dependent on the ratio A/P and the Q-factor of the passive resonator. Level curves are shown.
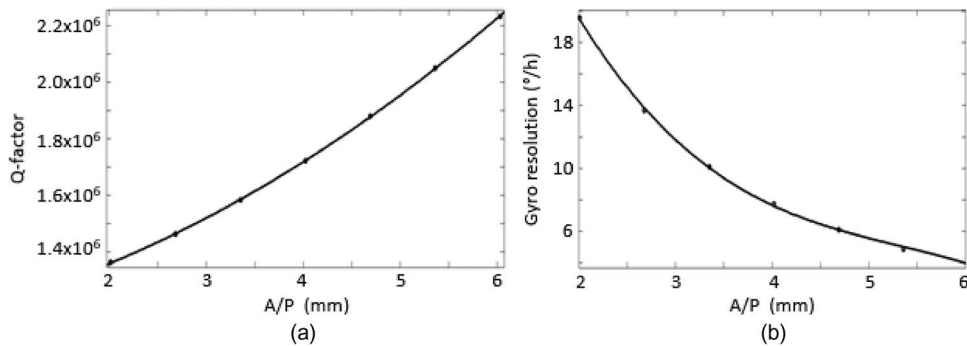

Fig. 19. (a) Q-factor dependence on the A/P ratio. (b) Gyro resolution vs. A/P.

The spiral resonator reported in this paper, with a footprint of approximately 10 mm², has $Q = 590\,000$ and $A/P = 0.67$ mm ($A = 40$ mm² and $P = 60$ mm). As shown by the blue point in Fig. 18, those values correspond to a shot noise limited resolution of 150 °/h, which is appropriate only for some application domains, such as automotive and robotics, which are already well covered by low-cost MEMS gyros. That performance can be improved by increasing the A/P ratio. The consequences of this strategy are an increase in the Q-factor, which has a positive influence on the gyro performance, and the enlargement of the sensor footprint. Since a too large footprint could imply a non-uniform fabrication process, there is a limit in the A/P increase. Based on our experience, we conclude that the sensor should fit in 1/4 of the 3-inch wafer to avoid critical aspects relevant to a non-uniform fabrication process. Therefore, we assume that the maximum value of A/P is approximately 6 mm.

By using the model in [48], for A/P ranging from 2 mm to 6 mm, we have calculated the resonator Q-factor, assuming the best waveguide propagation loss as demonstrated using the COBRA platform, i.e., 0.3 dB/cm [36], and an extinction ratio of the resonator spectral response equal to 8 dB. The result of this calculation is shown in Fig. 19(a). The Q-factor increases quite linearly

as A/P increases and for all A/P values considered the calculated value of Q improves on the state-of-the art, equal to 1.2×10^6 [36]. Data in Fig. 19(a) allow us to estimate, using (1), the gyro resolution depending on the A/P ratio [see Fig. 19(b)]. Based on that estimation, we can conclude that if A/P is increased by a factor of 5 up to 3.35 mm, designing a spiral resonator with the same shape as the fabricated one, but having a footprint of approximately 200 mm^2, the gyro will reach the target resolution, i.e., 10 °/h (see the blue star in Fig. 18). This scaled version of the spiral resonator with $A/P = 3.35$ mm, $Q = 1.58 \times 10^6$, footprint $= 200$ mm^2, and $\delta\Omega = 10$ °/h would improve the state-of-the-art of InP ring resonators [33] by about 30% and would be 3.4 times smaller than the InP resonator in [30], having a footprint of 680 mm^2, which enables the same sensor resolution of 10 °/h.

The experimental demonstration of the up-scaled version of the spiral resonators is surely challenging because a good uniformity of the fabrication process allowing a propagation loss of 0.3 dB/cm should be guaranteed over a quite large chip area of 200 mm^2.

The bias drift of the RMOG based on the resonant sensing element reported in this paper (footprint $= 10$ mm^2) can be estimated using the model reported in [49], assuming the nonlinear index coefficient of the material forming the waveguide core to be equal to 10^{-18} m^2/W, the waveguide effective area $= 3$ μm^2, and the drift in the difference between the optical powers of the resonant modes counter-propagating within the spiral cavity is equal to 10 nW. Under those assumptions, the bias drift is equal to 4 °/h. An RMOG based on the above-mentioned spiral cavity having footprint of about 200 mm^2 would exhibit a bias drift < 1 °/h.

6. Conclusion

Design, fabrication, and optical characterization of an InP resonant angular velocity sensor as the key building block of a monolithically integrated photonic gyro is reported in this paper. The fundamental advantage of this InP-based gyro sensing element is that the generic integration process which was selected for fabrication of the device is demonstrated to be extremely appropriate for the fully monolithic integration of the gyro.

The resolution of the gyroscope based on the designed sensor (footprint about 10 mm^2), which is a spiral cavity (Q-factor $= 590\,000$) coupled to a straight bus waveguide through an MMI coupler, is approximately 150 °/h, while its bias drift is a few °/h. This performance can be improved by up-scaling the spiral resonator up to a footprint of about 200 mm^2. In this way, the resolution becomes 10 °/h and the bias drift decreases down to about 1 °/h. This performance is then compliant with the typical requirements of some applications in the field of aerospace and defense, such as the autonomous navigation of planetary rovers or the attitude and orbit control of small satellites. We expect that a gyroscope including the up-scaled spiral resonator co-packaged with the miniaturized readout electronics would have a volume of a few cm^3, a weight of a few tens of grams, and a power consumption of a few Watts. This level of miniaturization, which today is achievable only by the low-performance MEMS gyros, could have an impressive enabling potential in many technological areas. The paper is the first demonstration, based on experimental evidence, that a photonic gyro-on-chip with resolution $= 10$ °/h is feasible through an InP-based generic integration process allowing the multi-project wafer option and having a mid-term target cost of only 10 €/mm^2.

References

[1] P. Fahlstrom and T. Gleason, *Introduction to UAV Systems*. Hoboken, NJ, USA: Wiley, 2012.
[2] *Small Spacecraft Technology State of the Art*, NASA/TP-2014-216648/REV1, Mission Design Division Staff Ames Research Center, Moffett Field, CA, USA, 2014. [Online]. Available: http://www.nasa.gov/directorates/spacetech/small_spacecraft/
[3] C. Ciminelli, F. Dell'Olio, C. E. Campanella, and M. N. Armenise, "Photonic technologies for angular velocity sensing," *Adv. Opt. Photon.*, vol. 2, no. 3, pp. 370–404, Sep. 2010.
[4] F. Dell'Olio, T. Tatoli, C. Ciminelli, and M. N. Armenise, "Recent advances in miniaturized optical gyroscopes," *J. Eur. Opt. Soc.*, vol. 9, 2014, Art. ID 14013.

[5] M. N. Armenise, C. Ciminelli, F. Dell'Olio, and V. M. N. Passaro, *Advances in Gyroscope Technologies*. Berlin, Germany: Springer-Verlag, 2010.

[6] R. Durrant, H. Crowle, J. Robertson, and S. Dussy, "SIREUS—Status of the European MEMS rate sensor," presented at the 7th Int. ESA Conf. Guidance, Navigation Control Syst., Tralee, Ireland, Jun. 2–5, 2008, Paper AIAA 2008-6992.

[7] S. Kowaltschek, "Lessons learnt from the SiREUS MEMS detector evaluation," in *Proc. 6th ESA/ESTEC Workshop Avionics Data, Control Softw. Syst.*, Noordwijk, The Netherlands, Oct. 23–25, 2012, pp. 1–16.

[8] W. Lawrence, "Thin film laser gyro," U.S. Patent 4 326 803, Apr. 27, 1982.

[9] O. Kenji, "Semiconductor ring laser gyro," JP Patent 60 148 185, Aug. 5, 1985.

[10] G. Sagnac, "L'èther lumineux dèmontrè par l'effet du vent relative d'èther dans un interfèromètre en rotation uniforme," *Comptes Rendus Acad. Sci.*, vol. 95, pp. 708–710, 1913.

[11] M. Armenise and P. J. R. Laybourn, "Design and simulation of a ring laser for miniaturised gyroscopes," in *Proc. SPIE*, 1998, vol. 3464, pp. 81–90.

[12] M. N. Armenise, M. Armenise, V. M. N. Passaro, and F. De Leonardis, "Integrated optical angular velocity sensor," EP Patent 1219926, Jul. 3, 2010.

[13] M. Osiński, H. Cao, C. Liu, and P. G. Eliseev, "Monolithically integrated twin ring diode lasers for rotation sensing applications," *J. Cryst. Growth*, vol. 288, no. 1, pp. 144–147, Feb. 2006.

[14] H. Ma, X. Zhang, Z. Jin, and C. Ding, "Waveguide-type optical passive ring resonator gyro using phase modulation spectroscopy technique," *Opt. Eng.*, vol. 45, no. 8, Aug. 2006, Art. ID 080506.

[15] T. Imai, K. Nishide, H. Ochi, and M. Ohtsu, "The passive ring resonator fiber optic gyro using modulatable highly coherent laser diode module," in *Proc. SPIE*, 1992, vol. 1585, 153–162.

[16] F. Dell'Olio *et al.*, "System test of an optoelectronic gyroscope based on a high Q-factor InP ring resonator," *Opt. Eng.*, vol. 53, no. 12, Dec. 2014, Art. ID 127104.

[17] H. Ma, Z. He, and K. Hotate, "Reduction of backscattering induced noise by carrier suppression in waveguide-type optical ring resonator gyro," *J. Lightw. Technol.*, vol. 29, no. 1, pp. 85–90, Jan. 2011.

[18] H. Ma, J. Zhang, L. Wang, and Z. Jin, "Double closed-loop resonant micro optic gyro using hybrid digital phase modulation," *Opt. Exp.*, vol. 23, no. 12, pp. 15088–15097, Jun. 2015.

[19] J. Wang, L. Feng, Y. Tang, and Y. Zhi, "Resonator integrated optic gyro employing trapezoidal phase modulation technique," *Opt. Lett.*, vol. 40, no. 2, pp. 155–158, Jan. 2015.

[20] H. C. Lefèvre, *The Fiber-Optic Gyroscope*. Norwood, MA, USA: Artech House, 2014.

[21] K. Suzuki, K. Takiguchi, and K. Hotate, "Monolithically integrated resonator microoptic gyro on silica planar lightwave circuit," *J. Lightw. Technol.*, vol. 18, no. 1, pp. 66–72, Jan. 2000.

[22] G. Li, K. A. Winick, B. R. Youmans, and E. A. J. Vikjaer, "Design, fabrication and characterization of an integrated optic passive resonator for optical gyroscopes," in *Proc. 60th Annu. Meet. Inst. Navig.*, Dayton, OH, USA, Jun. 7–9, 2004, pp. 211–216.

[23] R. E. Meyer, S. Ezekiel, D. W. Stowe, and V. J. Tekippe, "Passive fiber-optic ring resonator for rotation sensing," *Opt. Lett.*, vol. 8, no. 12, pp. 644–646, Dec. 1983.

[24] T. Imai, Y. Miki, S. Maeda, and K. Nishide, "Development of resonator fiber optic gyros," presented at the Opt. Fiber Sensors Conf., Sapporo, Japan, 1996, Paper Ex21.

[25] M. A. Terrel, M. J. F. Digonnet, and S. Fan, "Resonant fiber optic gyroscope using an air-core fiber," *J. Lightw. Technol.*, vol. 30, no. 7, pp. 931–937, Apr. 2012.

[26] H. Ma, X. Yu, and Z. Jin, "Reduction of polarization-fluctuation induced drift in resonator fiber optic gyro by a resonator integrating in-line polarizers," *Opt. Lett.*, vol. 37, no. 16, pp. 3342–3344, Aug. 2012.

[27] X. Yu, H. Ma, and Z. Jin, "Improving thermal stability of a resonator fiber optic gyro employing a polarizing resonator," *Opt. Exp.*, vol. 21, no. 1, pp. 358–369, Jan. 2013.

[28] J. Wu *et al.*, "Resonator fiber optic gyro with high backscatter-error suppression using two independent phase-locked lasers," in *Proc. SPIE*, 2015, vol. 9634, Art. ID 96341O.

[29] H. Mao, H. Ma, and Z. Jin, "Polarization maintaining silica waveguide resonator optic gyro using double phase modulation technique," *Opt. Exp.*, vol. 19, no. 5, pp. 4632–4643, Feb. 2011.

[30] C. Ciminelli, F. Dell'Olio, and M. N. Armenise, "Resonant optical gyro: Monolithic vs. hybrid integration," in *Proc. ICTON*, Cartagena, Spain, Jun. 23–27, 2013, pp. 1–4.

[31] M. K. Smit *et al.*, "An introduction to InP-based generic integration technology," *Semicond. Sci. Technol.* vol. 29, no. 8, Jun. 2014, Art. ID 083001.

[32] F. Dell'Olio, C. Ciminelli, and M. N. Armenise, "Theoretical investigation of InP buried ring resonators for new angular velocity sensors," *Opt. Eng.*, vol. 52, no. 2, Feb. 2013, Art. ID 024601.

[33] C. Ciminelli, F. Dell'Olio, M. N. Armenise, F. M. Soares, and W. Passenberg, "High performance InP ring resonator for new generation monolithically integrated optical gyroscopes," *Opt. Exp.*, vol. 21, no. 1, pp. 556–564, Jan. 2013.

[34] H. P. M. M. Ambrosius *et al.*, "A generic InP-based photonic integration technology," in *Proc. 23rd Int. Conf. Indium Phosphide Relat. Mater.*, Berlin, Germany, May 22–26, 2011, pp. 1–4.

[35] D. D'Agostino, "Capability extensions to the COBRA generic photonic integration platform," Ph.D. dissertation, Dept. Electr. Eng., Eindhoven Tech. Univ., Eindhoven, The Netherlands, 2015.

[36] D. D'Agostino *et al.*, "Low-loss passive waveguides in a generic InP foundry process via local diffusion of zinc," *Opt. Exp.*, vol. 23, no. 19, pp. 25143–25157, Sep. 2015.

[37] F. Fiedler and A. Schlachetzki, "Optical parameters of InP-based waveguides," *Solid State Electron.*, vol. 30, no. 1, pp. 73–83, Jan. 1987.

[38] W. Walukiewicz *et al.*, "Electron mobility and free-carrier absorption in InP; determination of the compensation ratio," *J. Appl. Phys.*, vol. 51, no. 5, pp. 2659–2668, May 1980.

[39] L. B. Soldano, "Multimode interference coupler design and application," Ph.D. dissertation, Dept. Electr. Eng., Delft Univ. Technol., Delft, The Netherlands, 1994.

[40] M. Bachmann, P. A. Besse, and H. Melchior, "Overlapping-image multimode interference couplers with a reduced number of self-images for uniform and nonuniform power splitting," *Appl. Opt.*, vol. 34, no. 30, pp. 6898–6910, Oct. 1995.

[41] Y. Liu, J. M. Shainline, X. Zeng, and M. A. Popovic, "Ultra-low-loss CMOS compatible waveguide crossing arrays based on multimode Bloch waves and imaginary coupling," *Opt. Lett.*, vol. 39, no. 2, pp. 335–338, Jan. 2014.

[42] F. Dell'Olio *et al.*, "Backscattering noise control in the readout circuit of innovative optoelectronic resonant gyroscopes," in *Proc. Fotonica AEIT Italian Conf. Photon. Technol.*, Naples, Italy, May 12–14, 2014, pp. 1–3.

[43] D. D'Agostino, D. Lenstra, H. P. M. M. Ambrosius, and M. K. Smit, "Coupled cavity laser based on anti-resonant imaging via multimode interference," *Opt. Lett.*, vol. 40, no. 4, pp. 653–656, Feb. 2015.

[44] D. D'Agostino, D. Lenstra, H. Ambrosius, and M. Smit, "Widely tunable coupled cavity laser based on a Michelson interferometer with doubled free spectral range," presented at the Opt. Fiber Commun. Conf., Los Angeles, CA, USA, 2015, Paper M2D.4.

[45] D. O. Dzibrou, J. J. G. M. van der Tol, and M. K. Smit, "Tolerant polarization converter for InGaAsP-InP photonic integrated circuits," *Opt. Lett.*, vol. 38, no. 18, pp. 3482–3484, Sep. 2013.

[46] L. Liu, J. Dong, D. Gao, A. Zheng, and X. Zhang, "On-chip passive three-port circuit of all-optical ordered-route transmission," Sci. Rep., vol. 5, May 2015, Art. ID 10190.

[47] T. Feuchter and C. Thirstrup, "High precision planar waveguide propagation loss measurement technique using a Fabry-Perot cavity," *IEEE Photon. Technol. Lett.*, vol. 6, no. 10, pp. 4–7, Oct. 1994.

[48] A. Yariv, "Universal relations for coupling of optical power between microresonators and dielectric waveguides," *Electron. Lett.*, vol. 36, no. 4, pp. 321–322, Feb. 2000.

[49] C. Ciminelli, F. Dell'Olio, and M. N. Armenise, "High-Q spiral resonator for optical gyroscope applications: Numerical and experimental investigation," *IEEE Photon. J.*, vol. 4, pp. 1844–1854, Oct. 2012.